Journal of Materials Research and Technology 30 (2024) 2333–2346

Contents lists available at ScienceDirect

Journal of Materials Research and Technology

journal homepage: www.elsevier.com/locate/jmrt

Surface modification of $Ti_{40}Cu_{40}Zr_{11}Fe_3Sn_3Ag_3$ amorphous alloy for enhanced biocompatibility in implant applications

Kirti Tiwari [a], Andreu Blanquer [b], Cristina Pavan [c,d,*], Maura Tomatis [c,e], Nora Fernandez Navas [f,g], Federico Scaglione [a], Gianluca Fiore [a], Francesco Turci [c], Carme Nogués [b,**], Paola Rizzi [a]

[a] Department of Chemistry and NIS, Università degli Studi di Torino, 10125, Torino, Italy
[b] Departament de Biologia Cel·lular, Fisiologia i Immunologia Universitat Autònoma de Barcelona Edifici C, 08193, Bellaterra, Spain
[c] Department of Chemistry, "G. Scansetti" Interdepartmental Centre for Studies on Asbestos and Other Toxic Particulates, Università degli Studi di Torino, 10125, Torino, Italy
[d] Louvain Centre for Toxicology and Applied Pharmacology, Institute of Experimental and Clinical Research, Université catholique de Louvain, 1200, Brussels, Belgium
[e] Department of Veterinary Sciences, Università degli Studi di Torino, 10095, Grugliasco, Italy
[f] Leibniz Institute for Solid State and Materials Research Dresden (Leibniz IFW Dresden), 01069, Dresden, Germany
[g] Faculty of Mechanical Science and Engineering, TU Dresden, 01069, Dresden, Germany

ARTICLE INFO

Keywords:
Amorphous alloy
Biomedical implant
Ti based alloy
Dealloying
Hemocompatibility
Biocompatibility
Surface treatment

ABSTRACT

This study focuses on the design of a new Ti based multicomponent amorphous alloy for the development of biocompatible implant materials with enhanced hemocompatibility and cytocompatibility. While this class of amorphous alloys has shown its potential for biomedical implant applications, there are major concerns due to the presence of elements such as copper which can lead to cytotoxicity in the human body during long term implantation. Nevertheless, copper is indispensable in the development of an amorphous alloy. Thus, the objective of this work is to selectively remove copper from the surface of the $Ti_{40}Cu_{40}Zr_{11}Fe_3Sn_3Ag_3$ (at%) amorphous alloy using the dealloying technique and produce a patterned protective passivated surface rich in Ti and Zr oxides. Nitric acid (HNO_3) has been found to be effective in depleting copper from the sample surface. Optimization of treatment parameters such as temperature (70 °C and room temperature) yielded drastic differences in the morphology of the samples studied using Field-Emission Scanning Electron Microscopy. The treated sample surface demonstrated good hemocompatibility and cytocompatibility with primary human osteoblast cells (HOb) and human osteosarcoma cell line (Saos-2). Additionally, the treated samples showed higher ability to produce reactive oxygen species with respect to pristine samples, which could be convenient for preserving the implant from bacterial contamination. These findings contribute to the advancement of producing copper-depleted nanostructured Ti based amorphous alloys for biomedical implant applications.

1. Introduction

Amorphous alloys are a unique class of advanced materials, offering a combination of properties that make them attractive for a wide range of applications [1]. Titanium based amorphous alloys are promising as compared to crystalline alloys, due to their unique combination of properties, such as mechanical strength, low thermal expansion, enhanced elastic limit, wear and corrosion resistance, making them suitable for use in medical implants [2]. They also have the potential to be used in medical devices, including stents, due to their biocompatibility, flexibility, and low thermal expansion [3].

In the past decades researchers are focusing on developing amorphous alloys with compositions containing biocompatible elements such as Ti, Zr, Pd [4–8]. Wang et al. studied the biocompatibility of $Ti_{41.5}Zr_{2.5}Hf_5Cu_{37.5}Ni_{7.5}Si_1Sn_5$ amorphous alloy and commercially pure Ti, using in vitro cell response and in vivo animal response. The results

* Corresponding author. Department of Chemistry, "G. Scansetti" Interdepartmental Centre for Studies on Asbestos and Other Toxic Particulates, Università degli Studi di Torino, 10125, Torino, Italy.
** Corresponding author.
E-mail addresses: cristina.pavan@unito.it (C. Pavan), carme.nogues@uab.cat (C. Nogués).

https://doi.org/10.1016/j.jmrt.2024.03.225
Received 12 December 2023; Received in revised form 9 February 2024; Accepted 28 March 2024
Available online 30 March 2024

indicated that the two materials were well integrated with a gap less than 5 μm between bone tissue and implant after one month post-implantation. However, presence of Ni and high content of Cu was considered concerning [9], and suggested the necessity to evaluate the biocompatibility of $Ti_{41.5}Zr_{2.5}Hf_5Cu_{37.5}Ni_{7.5}Si_1Sn_5$ amorphous alloy for long-term implantation. Liu et al. studied the cytocompatibility of three different Ti–Zr–Cu–Fe–Sn–Si amorphous alloys and Ti6Al4V alloy with mouse pre-osteoblast MC3T3-E1 and found that cell viability in the $Ti_{47}Zr_{7.5}Cu_{40}Fe_{2.5}Sn_2Si_1$ amorphous alloy extracts was slightly higher than that in the Ti6Al4V alloy extract [10]. Yang et al. reported that (Ti, Zr,Cu)$_{92.5}Fe_{2.5}Sn_2Si_1Ag_2$ amorphous alloy showed moderate bio-corrosion resistance and good biocompatibility with MC3T3-E1 cells in a direct and indirect in vitro cell culture [11]. Kokubun et al. conducted an in vivo evaluation of $Ti_{40}Zr_{10}Cu_{34}Pd_{14}Sn_2$ amorphous alloy and found that it showed biocompatibility and integration to bone tissue, with no abnormal findings or inflammation detected up to three months post-implantation [12]. Despite these advantages, amorphous alloys with high copper concentration are observed to suffer from wear, localized corrosion, and cytotoxicity [13]. Therefore, it is important to modify the surface of the implant material (chemical composition, morphology, and roughness) for improving biocompatibility and reducing the risk of adverse reactions [14–19]. Dealloying is a simple and less explored technique which can be used to produce unique morphology and surface properties [20,21]. Additionally, it can selectively remove harmful or undesirable elements from the surface of the alloy. While this technique is facile, it faces some challenges such as controlling the dissolution rate of each element in the alloy. In this respect, it is important to carefully tailor the process parameters such as temperature, time, and composition of the electrolyte [22]. Several attempts have been made in literature to chemically/electrochemically treat Ti–Cu based alloys to reduce their copper content. The reaction of nitric acid with copper has been discussed widely in the literature [23–26]. As shown in reaction I (eqs (1) and (2)), both copper and cuprous oxide react with nitric acid and oxidizes to Cu^{2+} generating copper nitrate that can be released in the electrolyte. The selective dissolution of copper atoms from the surface enables the surface diffusion of remaining atoms, mainly titanium, at the surface-electrolyte interface, allowing the atoms to rearrange and modify the surface morphology. It is also reported in literature that the exposed atom of Ti can react with nitric acid, as shown in reaction II (eqs (3) and (4)), forming hydrated titania [27], which further decomposes to form stable titanium dioxide [28,29].

I. Reaction of Copper in nitric acid

$$Cu_2O + 6HNO_3 \rightarrow 2Cu(NO_3)_2 + 2NO_2 + 3H_2O \quad (1)$$

$$Cu + 4HNO_3 \rightarrow Cu(NO_3)_2 + 2NO_2 + 2H_2O \quad (2)$$

II. Reaction of Titanium in nitric acid

$$Ti + 4HNO_3 \rightarrow H_2TiO_3 + 4NO_2 + H_2O \quad (3)$$

$$H_2TiO_3 \leftrightarrow TiO_2 + H_2O \quad (4)$$

S. Zhu et al. reported that dealloying of copper from a $Ti_{40}Cu_{60}$ at% amorphous alloy, using nitric acid (13.14 M) at 70 °C resulted in the formation of a dealloyed layer with thickness around 3–5 μm. Additionally, the authors reported the formation of a titanium oxide rich layer on the sample surface [30]. In another study by S.L. Zhu et al. it is reported that a nanoporous layer on the surface of $Ti_{30}Cu_{70}$ at% glassy alloy was produced by using 5.36 M of HNO_3, at 1.0 V, for 3 h at 70 °C. The nanoporous layer thickness was 100 nm and it was composed of TiO, Ti_2O_3, TiO_2 and Cu_2O [31]. A limited penetration depth in dealloying of Ti–Cu based amorphous alloys is usually observed due to the rapid oxidation of the surface which inhibits surface diffusion and removal of atoms. Due to such limitations, the Ti–Cu based systems are not prone to undergo complete dealloying in bulk as observed in gold, silver, and platinum alloys [20,32,33]. Therefore, it is possible to describe the process as a pseudo-dealloying with a change that remains limited to a surface layer [34].

In a recent study Wang et al. conducted an investigation into the glass-forming ability (GFA) of $Ti_{46}Cu_{31.5-x}Zr_{11.5}Co_3Si_1Ag_x$ alloy by varying the silver (Ag) content (x) from 0 to 5 at%. The addition of 4 at% of Ag led to the formation of a fully amorphous state with no crystallites, indicating that Ag improves GFA by decreasing the melting temperature and enhancing the activation energy of crystallization [35]. Zr and Sn are known to enhance the ability to form glassy alloys, and numerous amorphous alloys have been developed with significant contributions from Zr and Sn [36–38], which can be attributed to the mismatch in atomic sizes between Ti (0.147 nm), Cu (0.16 nm), Zr (0.128 nm), and Sn (0.14 nm) [39]. These atomic size differences introduce complexity and disrupt crystalline phases during the melting process. Recently, Pang et al. reported a newly developed amorphous alloy, i.e., $Ti_{47}Cu_{38}Zr_{7.5}Fe_{2.5}Sn_2Si_1Ag_2$ (at%), with a critical diameter of 7 mm, exhibiting a Young's modulus of approximately 100 GPa, similar to the Ti6Al4V alloy. This amorphous alloy composition demonstrated a favorable combination of mechanical properties (compressive strength of $\sigma_{max} = 2080$ MPa) and compatibility with MC3T3-E1 osteoblast cells [40]. Additionally, $Ti_{47}Cu_{38}Zr_{7.5}Fe_{2.5}Sn_2Si_1Ag_2$ amorphous alloy exhibited superior wear resistance compared to Ti6Al4V and was comparable to Co28Cr6Mo in air. While in phosphate buffered solution, this amorphous alloy demonstrated better wear resistance than Ti6Al4V but slightly inferior to Co28Cr6Mo [41]. The corrosion rate of this amorphous alloy in phosphate buffered solution at 37 °C was 6.5×10^{-4} mm/year, which was similar to Ti6Al4V (6.8×10^{-4} mm/year) [42]. The primary causes of pitting corrosion in Ti–Cu-based and Zr–Cu-based amorphous alloys are attributed to the high copper content. The occurrence of pitting corrosion poses a notable challenge for the prolonged functionality of these materials and it is likely to result in premature failure of implants [43–45]. To address this concern, a potential approach involves emphasizing improved surface oxidation to minimize the leaching of copper ions into the surrounding physiological environment, thereby reducing the potential for inflammatory responses or cell death [34,46].

Ti-based alloys and copper oxides may generate Reactive Oxygen Species (ROS) which are highly reactive species that could lead to detrimental cellular effects when overproduced. Among ROS, hydroxyl radical ($^{\bullet}OH$) is one of the most abundant specie involved in cell damage induced by different types of materials [47] and some of the components of our alloy could provide $^{\bullet}OH$ radicals by the Fenton reaction, including, Ti-based compounds, and redox-active metal transition ions, such as copper and iron [48]. Besides chemical composition, other alloy properties such as surface roughness, porosity, mechanical properties, which affect the extent of the exposed surface and the corrosion resistance, may influence $^{\bullet}OH$ radical generation [49]. The $^{\bullet}OH$ radicals can react with a vast range of biomolecules, such as lipids, proteins, and nucleic acids. Because of their high oxidizing potential, $^{\bullet}OH$ radicals are very deleterious to cell membranes, organelles, and tissues in biological systems [50]. The $^{\bullet}OH$ radicals produced by the implanted material can, on one side, damage bacteria membranes and hinder their attachment to implant surfaces, thus reducing implant rejection due to biofilm formation and increasing the biocompatibility of the material [51,52]. On the other hand, if $^{\bullet}OH$ radical production is excessive, it may reduce cell adhesion and viability, possibly impairing osseointegration [53]. Indeed, elevated $^{\bullet}OH$ radical levels can have detrimental effects on osteoblast activity, leading to a reduction in extracellular matrix synthesis and mineralization, and potentially osteoblast cell death. Demonstrating the safety and cytocompatibility of these alloys is an essential prerequisite for their consideration as potential biomaterials for medical applications [54]. Therefore, in order to assess the biocompatibility of new Ti-based alloys, it is of importance to evaluate the $^{\bullet}OH$ radical production and cytocompatibility, and to tailor the

material surface morphology and chemistry to control mechanisms of cell damage. One of the requirements for implants in contact with blood is to not cause acute hemolysis, i.e., to be hemocompatible. For instance, 316 L-stainless steel and commercially pure titanium are considered hemocompatible, and a recent study comparing the commercially pure titanium and Ti–8Mo–2Fe materials showed that Ti–8Mo–2Fe alloy did not cause hemolysis [55]. Ti–Nb–Zr–Si thin film metallic glass showed enhanced hemocompatibility with respect to the Ti6Al4V specimen [56]. Thus, Ti-based amorphous alloys appear as good candidate in terms of blood compatibility.

The current study focuses on designing a novel amorphous alloy with the composition $Ti_{40}Cu_{40}Zr_{11}Fe_3Sn_3Ag_3$ at%. The concentrations of Ti, Sn, Zr, and Cu were adjusted to enhance the GFA, especially by maintaining a high (Ti + Zr)/Cu ratio (=1.28) and increasing the Sn content to potentially expand the supercooled liquid region. Surface modifications were undertaken to improve biocompatibility and control $^{\bullet}OH$ radical production for an effective antibacterial activity. In detail, pseudo-dealloying using nitric acid was performed on a $Ti_{40}Cu_{40}Zr_{11}Fe_3Sn_3Ag_3$ at% amorphous alloy. The evolution of the surface morphology was investigated by altering treatment parameters such as time and temperature of dealloying. The wettability and release of $^{\bullet}OH$ radical were evaluated in a cell-free system. Furthermore, hemocompatibility was measured using sheep's defibrinated blood, and cytocompatibility of the samples was studied using two human osteoblast cell lines (Saos-2 and HOb).

2. Materials and methods

2.1. Material preparation and pseudo-dealloying

Amorphous ribbon with composition $Ti_{40}Cu_{40}Zr_{11}Fe_3Sn_3Ag_3$ (at%) was prepared using planar flow casting technique. Pure elements (Ti, Cu, Zr, Fe, Sn, Ag) were arc melted to develop the master alloy ingot. Further the ingot was rapidly quenched on a rotating copper wheel to produce amorphous ribbons of 0.4 cm width and 50 μm thickness. The structure of the amorphous ribbon sample was analyzed using a X-ray diffraction (XRD) instrument Panalytical X'Pert, using Cu Kα radiation (λ = 1.5418 Å) in Bragg Brentano geometry and continuous mode. Current of 30 mA and tension of 40 kV was used. The slit sizes were 1/4° and 5 mm, measurements were recorded for 600 counts and 0.0167 step size.

Pseudo-dealloying was performed on amorphous ribbon using 14.6 M HNO_3 at room temperature (RT) for 2 months and at 70 °C for 24, 48, 72 h using a water bath, similar to a procedure used in literature [57]. Before pseudo-dealloying treatment, ribbon samples were ultrasonically cleaned for 5 min in acetone and ethanol followed by air drying. After the treatment, ribbons were rinsed with double distilled water for five times and dried using oven at 50 °C for 12 h to ensure removal of residual electrolyte and water from the ribbon surface. Later the samples were stored in ambient conditions.

2.2. Surface characterization

The morphology and chemical composition of treated ribbon was characterized using a TESCAN Vega 4, Scanning Electron Microscope (SEM) equipped with Ultim Max 40 mm^2 Oxford instrument electron dispersive spectroscopy (EDS). TESCAN S 9000 G Field Emission Scanning Electron microscope (FESEM) was used to analyze the morphology of the ribbons. Image J software was used to calculate the pore diameter and ligament size of the pseudo-dealloyed ribbons.

The cross section of the sample was analyzed by in-situ cutting using a Focused Ion Beam (FIB) inside the FESEM (FIB Helios 5 CX, Thermo Scientific). Auger electron spectroscopy (AES) was used for determining the chemical composition of the sample surface. Additionally surface depth profiling of the samples was performed, using a JEOL JAMP 9500F with Ar ions of 1 keV at 30° angle. The sputtering rate was measured using a reference sample, i.e., 6 nm/min (SiO_2 deposited on Si wafer). The AES measurements were performed with 10 KV and 10 nA beam condition. All sample surfaces were sputter cleaned for 30 s prior to AES measurements to remove adventitious carbon contamination.

Surfaces were imaged using amplitude modulation atomic force microscopy (AFM) (MFP-3D, Asylum Research) operated with Si probes (NCH, Nanosensors) having a nominal spring constant of 42 N/m and resonance frequency of 330 kHz. One representative image at 10 × 10 μm is shown from images collected in multiple locations. For presentation, images were flattened to remove sample tilt, horizontal correction was applied if required.

2.3. Contact angle

The wettability of the ribbons was analyzed using a Theta Lite optical tensiometer, Biolin Scientific Goniometer. The contact angle was measured on freshly prepared ribbons using 3 μL of solvent in sessile drop mode after 1 s of placing the drop. Two solvents were used for contact angle measurements and surface free energy (SFE) calculations, i.e., deionized water as polar solvent and diiodomethane as non-polar solvent. The SFE was calculated using Owens, Wendt, Rabel and Kaelble method (OWRK) and Young's equation. OneAttension software was used to measure the contact angle. This analysis was performed on the air side of the ribbons with a minimum of 3 measurements on each ribbon produced in triplicate.

2.4. Hemocompatibility

The hemocompatibility of the ribbons (0.4 × 3 cm) was evaluated according to ISO-10993-4 (2017) standards [35], using commercial defibrinated sheep blood (Microbiol). The blood was diluted with 10 mM phosphate buffer solution (PBS, Merck) in 4:5 ratio and calibrated using a positive control of 0.2 mL diluted blood in 10 mL of double distilled water (Merck-Millipore). The absorbance (Abs) of the positive control was adjusted to 0.9–1.0 by adding PBS or blood. The absorbance of the released hemoglobin (Hb) was measured at 540 nm using a UV/vis spectrophotometer (Uvikon, Kontron Instruments). A negative control with 10 mL of PBS and 0.2 mL diluted blood was additionally prepared. Commercially purchased Mg alloy (Mg93/Y4/Nd3 (WE43B, Goodfellow)), and quartz particles (Min-U-Sil 5, U.S. Silica, 200 cm^2/mL, and specific surface area of 5 m^2/g) were used as a positive reference material. Commercially pure titanium (cp-Ti) was used as a negative reference material. The samples were sterilized with 70% ethanol, further washed with double distilled water and PBS. The samples were immersed in 10 mL of PBS and pre incubated at 37 °C for 30 min. Further, 0.2 mL of diluted blood was added into test tubes and incubated at 37 °C for 60 min. After incubation, the solution of each tube was centrifuged at 500 g (Centrifuge Rotina 380R) for 5 min. The percentage of hemolysis was calculated using equation (5).

$$\%\ \text{Hemolysis} = \frac{\text{Abs(test)} - \text{Abs(negative control)}}{\text{Abs(positive control)} - \text{Abs(negative control)}} \times 100 \quad (5)$$

Hemoglobin adsorption by the samples was investigated using purified red blood cells (RBC). The absorbance of the hemolyzed blood was adjusted to 0.9–1 and a final volume of 10.2 mL of blood in PBS was frozen in the fridge at −20 °C overnight and defrosted to obtain lysed RBC. Then, the solution was centrifuged at 10,000 g for 10 min. The supernatant solution containing Hb was recovered. The samples were incubated in the solution containing Hb for 60 min at 37 °C. After the incubation, the absorbance of the Hb was measured. The measurements were performed in triplicate.

2.5. Hydroxyl radical generation

Generation of $^{\bullet}OH$ radicals was evaluated using the spin trapping technique coupled with electron paramagnetic resonance (EPR)

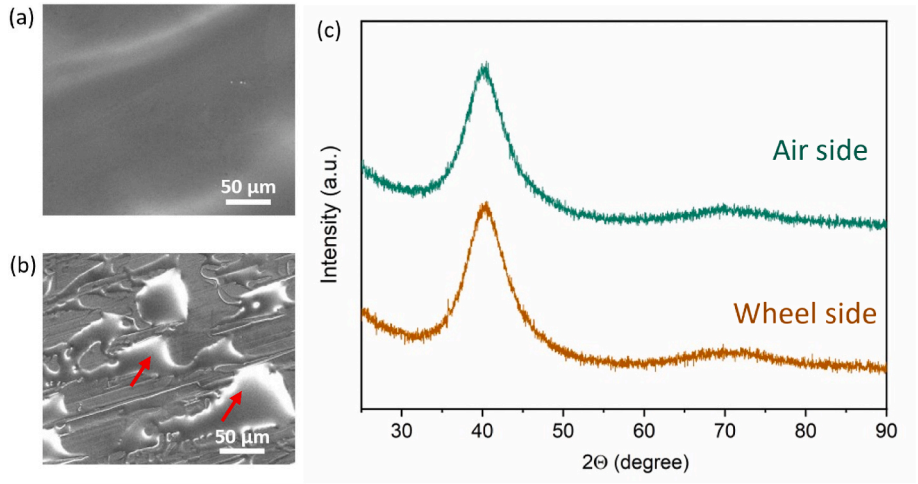

Fig. 1. SEM micrographs of as-quenched ribbon showing (a) air side and (b) wheel side (arrows indicating air pockets). XRD pattern (c) air side and wheel side.

spectroscopy. In this study, we optimized experimental conditions to enhance the detection of surface reactivity in cell-free assays.

The samples were ultrasonically cleaned using acetone followed by 70% ethanol for 10 min. Ribbon samples (0.4 × 1 cm) were immersed in 375 µL of 0.13 M H_2O_2 and 0.33 M phosphate buffer (PB, Sigma-Aldrich), pH = 7. The concentration of H_2O_2 mimics oxidative stress levels found in inflamed cells, exceeding typical concentrations in healthy tissues. The ribbons were incubated in a thermostatic shaker at 37 °C in the dark for 10 min. Following the incubation, an aliquot (180 µL) of the supernatant from each group was separated. The effect of 10 min contact with this oxidizing environment, which mimics what can be found in inflamed tissue, on the ability to generate •OH radicals was evaluated on both the supernatant and the ribbon samples. Then, 125 µL of 0.17 M 5,5-dimethyl-1-pyrroline-1-oxide (DMPO, Cayman Chemical Company), used as spin trap molecule, was added to the ribbons and the supernatant. The mixtures were again incubated in a thermostatic shaker at 37 °C in the dark. The final concentration of reagents in the solution was DMPO 0.07 M, PB 0.2 M and, H_2O_2 0.06 M, pH = 7. The pH = 7 was chosen, instead of the more acidic pH usually found in inflamed tissues, to avoid a decrease in signals that can be observed at acidic pH due to the lower stability of DMPO. EPR spectra was recorded by collecting an aliquot of the solution in a capillary at time point (0), 10, 30 and, 60 min of incubation. The kinetics of •OH radical release was studied until 60 min after DMPO addition, due to the rapid degradation of DMPO. Miniscope MS100 (Magnettech) with modulation of 1000 mG, scan range of 120 G, attenuation 7 dB and center of field at 3330 G was used for measuring EPR spectra. A negative control was prepared without the ribbon samples. All the measurements were performed in duplicates. The concentration of released •OH radical was calculated by double integration of the EPR spectra (Fig. 1 SI) using OriginPro 2023b software.

2.6. Ion release

The ribbons (0.4 × 0.6 cm) were immersed in DMEM (Dulbecco modified eagle medium, Gibco, ThermoFisher Scientific) cell culture media without cells for 3 days at 37 °C for ion release study. Later, aliquots of 1 mL were collected for analyzing ions released in the media using inductively coupled plasma mass spectrometry (ICP-MS) Agilent ICP-MS, model 7900. The study was performed with 3 replicates and compared with blank which was cell culture media without ribbon.

2.7. Cytocompatibility

2.7.1. Cell lines and cell culture

The ribbons (0.4 × 0.6 cm) were sterilized using absolute ethanol for 5 min, and glass coverslips of 1.5 cm diameter were used as control. The experiments were performed in triplicate.

Two different cell lines were used in this study: the human Saos-2 infinite cell line, derived from a human osteosarcoma (ATCC collection), and the finite cell line HOb obtained from healthy human donors. Both cell lines were cultured in DMEM supplemented with 10% (Saos-2 cells) or 20% (HOb cells) of FBS (fetal bovine serum, Gibco) and incubated at 37 °C and 5% CO_2. The ribbons were seeded with 50,000 Saos-2 cells per mL or with 20,000 HOb cells per mL in a 24 well plate.

2.7.2. Cell viability assay

The cytotoxicity of ribbons was evaluated at day 3 using live/dead kit for mammalian cells (Invitrogen) following manufactures protocol. Calcein was used to stain live cells (green) and ethidium bromide was used to stain dead cells (red). The stained ribbons were observed using an inverted fluorescent microscope (Olympus IX71). The images were processed using ImageJ software and percentage of cell viability was determined.

2.7.3. Cell morphology

The morphology of the adhered cells to the ribbons at day 3 of culture was analyzed using FE-SEM (Merlin; Zeiss). The samples were rinsed with PBS and fixed in 4% paraformaldehyde for 20 min at RT. The samples were later rinsed with PBS and dehydrated using gradient of ethanol ranging from 50, 70, 90 and 100% for 10 min each. Finally, the samples were dried using hexamethyl-di-silazane (Electron Microscopy Sciences) for 10 min. The samples were sputter coated with gold before imaging.

2.7.4. Cell adhesion

Cell adhesion and cytoskeleton organization of cells growing on ribbons was investigated after 3 days in culture. The cytoskeleton was visualized by staining actin filaments using phalloidin. After incubation, the cells were fixed with 4% paraformaldehyde for 20 min, followed by immersion in 0.1% Triton for 15 min and later in 1% TWIN for 20 min at RT. Samples were then immersed in 1% PBS-BSA for 20 min at RT. Further, cells were stained by immersing in a mixture of Phalloidin-Alexa 594 (ThermoFisher Scientific), and Hoechst 33258 (Sigma-Aldrich) for 1 h at RT. Finally, cells were washed with PBS and analyzed using confocal laser scanning microscope (CLSM, Leica SP5). The images were processed using Imaris viewer 9.9.1 software.

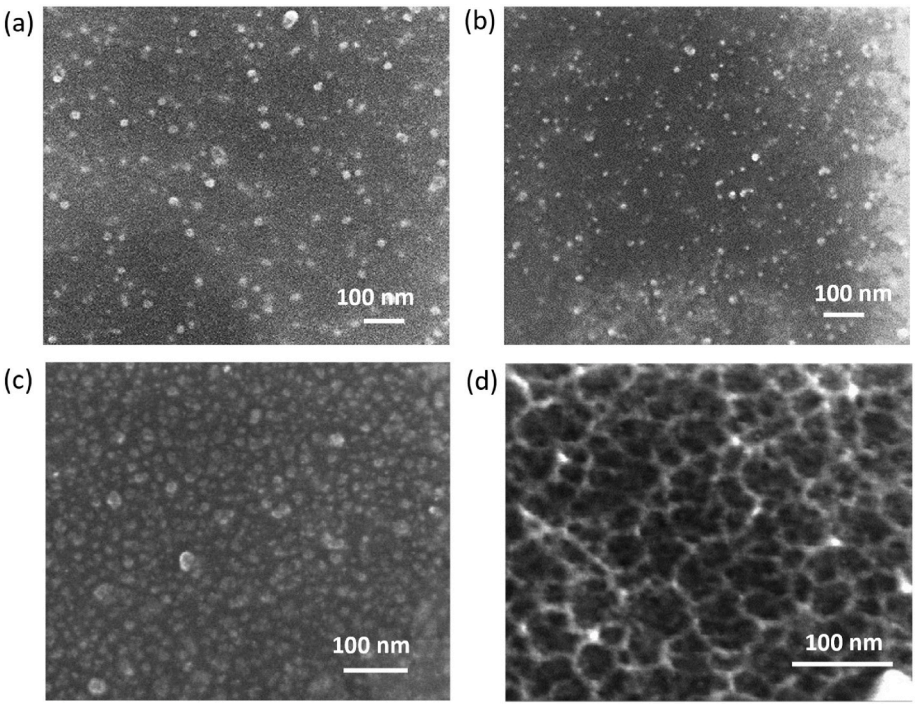

Fig. 2. FESEM images of pseudo-dealloyed ribbon samples in 14.6 M HNO_3 for (a) 24 h, (b) 48 h, (c) 72 h at 70 °C and (d) 2 months at RT.

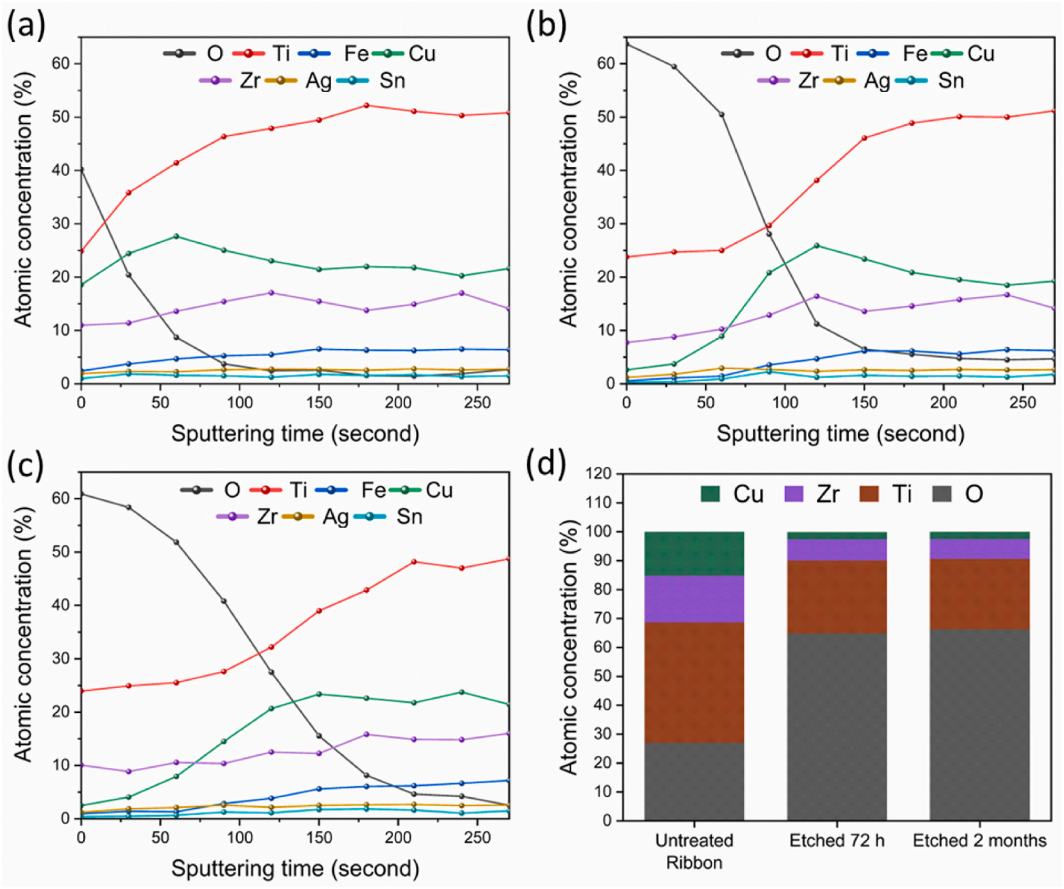

Fig. 3. Auger electron spectroscopy (AES) measurements (a) depth profiling of untreated ribbon, (b) depth profiling of etched 72 h ribbon sample, (c) depth profiling of etched 2 months sample, (d) quantified surface analysis of untreated, etched 72 h and etched 2 months ribbon sample for Ti, Cu, Zr, O elements.

2.7.5. Cell proliferation

The Alamar blue assay kit (Thermofisher Scientific) was used to investigate proliferation after day 1, 3, 7 of incubation of cells on ribbons. On day 1, ribbons with adhered cells were transferred to new wells. Then, samples were incubated in a mixture of cell media and Alamar blue reagent (10:1 dilution) for 4 h in dark condition at 37 °C and 5% CO_2. A negative control without sample was prepared as a standard reference. After the incubation period, supernatant was collected, and fluorescence was measured at 585 nm with excitation wavelength at 560 nm using a Varian Cary Eclipse Fluorimeter (Agilent Technologies, Santa Clara, CA, USA). The same procedure was performed on day 3 and 7 of cell culture. Media was changed after each time point of study. The data were normalized to day 1.

2.7.6. Cell differentiation

Cell differentiation was investigated by assessing the ALP (i.e., alkaline phosphatase) activity. The cells were incubated on the ribbon and, after 7 and 14 days, the incubated cells were lysed in CyQuant cell lysis buffer (Thermo Fisher Scientific) by transferring the samples to eppendorf tubes and subjecting them to 10 min of lysis, followed by 10 s of vortexing. The resulting cell lysates were then centrifuged at 12,000 rpm for 4 min at 4 °C, and the supernatants were collected. To measure ALP activity, the hydrolysis of *p*-nitrophenyl phosphate (pNPP) was employed, leading to the production of *p*-nitrophenol (pNP). Specifically, 25 μL of 1-step pNPP (Thermo Fisher Scientific) was mixed with 25 μL of the collected supernatant. The absorbance at 405 nm was measured using a Nanodrop Spectrophotometer (Thermofisher Scientific).

2.8. Statistical analysis

Data are presented as the mean ± standard error of the mean (SEM) unless otherwise stated. Normally distributed data were analyzed by one-way ANOVA or two-way ANOVA followed by Dunnett's or Tukey's post hoc test. A 95% confidence interval was applied, and values with $P < 0.05$ were deemed statistically significant, unless otherwise stated. The GraphPad Prism 8.0.2 software was used for conducting statistical analysis.

3. Results and discussion

3.1. Characterization of the as-quenched ribbon

The amorphous ribbons were prepared by melt spinning technique which involves rapid quenching of molten liquid of alloy on a rotating copper wheel. This results in formation of amorphous ribbons with two sides: wheel side, which is formed in contact with the rotating wheel, and air side, which is the free side. The morphology of the two sides differs because during rapid quenching the wheel side of the ribbon adapts to the roughness of the wheel and the gas that remains entrapped between the liquid melt and the wheel produces air pockets [58]. Compared to the wheel side, the air side has a slightly slower quenching rate, and it results in smooth and wavy morphology on the surface [59], as observed by SEM (Fig. 1 (a), (b)). The structure of the ribbon was analyzed using XRD (Fig. 1 (c)) and the XRD patterns, characterized by a broad diffraction peak on wheel side and air side, confirm the formation of a fully amorphous structure. Additionally, the composition of the as-quenched sample was verified by EDS to be $Ti_{40}Cu_{40}Zr_{11}Fe_3Sn_3Ag_3$ (at%), in accordance with the nominal composition (Fig. 3 SI). EDS elemental map (not shown) was performed confirming the homogeneous distribution of the elements in the sample, which is typical of an amorphous phase.

3.2. Pseudo-dealloying using nitric acid

Ribbons were subjected to different treatments to investigate the influence of temperature and treatment duration on morphology. The tests included immersion in a 14.6 M HNO_3 solution at 70 °C for 24, 48, and 72 h, as well as at RT for an extended period of 2 months. Fig. 2(a–d) displays the FESEM images of these ribbons.

Under the conditions of elevated temperature (70 °C), surface morphology was examined through FESEM. The progression of immersion time correlated with the formation of distinct hilly and globular structures. Upon a 24-h treatment (Fig. 2 (a)), small hills became apparent, and these features became more pronounced as the immersion time increased to 48 h (Fig. 2 (b)). After 72 h (Fig. 2 (c)), the surfaces displayed homogeneous and dense hilly structures, with an average diameter of 18 ± 3 nm and a separation distance of 27 ± 7 nm. Additionally, the 72 h treated ribbons exhibited more pronounced island-like structures compared to the 24 h and 48 h treated ribbons. Conversely, the ribbon immersed at RT for an extended period of 2 months exhibited different surface morphology when compared to ribbons treated at elevated temperatures (Fig. 2 (d)). This morphology was characterized by the presence of porosities with interconnected ligaments, which became evident upon high-magnification observation. Specifically, the 2-month-immersed ribbon revealed ligaments with an average thickness of 8 ± 2 nm and pores measuring 22 ± 6 nm in diameter.

The observation suggests a temperature-dependent influence on the removal of copper atoms from the surface. It was observed in literature, that surface diffusivity increases with increasing the temperature of the dealloying solution [60]. Hence it can be inferred that elevated temperature such as 70 °C facilitates the rearrangement of surface atoms through diffusion. This atomic rearrangement process leads to the formation of clusters that exhibit vertical growth, eventually culminating in the development of hilly surface structures. Conversely, when the ribbon is immersed in nitric acid at RT, the slower rate of surface diffusion results in the creation of fine pores and interconnected ligaments. The selective dissolution of copper, as well as minor species such as iron (Fe) and tin (Sn), initiates from the ribbons surface. This selective dissolution process allows the remaining atoms of titanium and zirconium to rearrange via surface diffusion at the surface-electrolyte interface. Notably, these exposed Ti and Zr atoms undergo simultaneous reactions with the surrounding medium, resulting in the formation of stable oxides [28,29].

Additionally, formation of brown gas within the sample holder was observed. The presence of this brown gas suggests the evolution of NO_2 gas (Fig. 2 SI), which is a noteworthy byproduct of the dissolution process [30]. Hereafter the as-quenched ribbon sample is referred to as "untreated ribbon" and ribbon treated for 72 h at 70 °C and 2 months at RT will be named as "Etched 72 h" and "Etched 2 months" respectively.

The chemical composition of the untreated and etched 72 h and etched 2 months ribbon samples were analyzed using Auger Electron Spectroscopy (AES) to determine the chemical composition on the surface, along with sputter depth profiling using Ar ions (6 nm/min for SiO_2 reference sample). The untreated ribbon sample (Fig. 3 (a)) shows evidence of a native oxide layer on the surface of around 7 nm thick composed of Ti, Cu and Zr. The etched 72 h ribbon sample (Fig. 3 (b)) shows an enrichment in O, Ti and Zr on the surface, while Cu is significantly depleted with respect to the untreated ribbon, indicating the formation of a mixed oxide layer of Ti and Zr. The content of Cu gradually increases until 125 s of sputtering time (i.e. around 12 nm of thickness), while the oxygen is reduced after 150 s indicating that the layer formed due to pseudo-dealloying is about 15 nm. A similar behaviour is observed for the etched 2 months ribbon sample (Fig. 3 (c)) in which the surface shows an enrichment in O, Ti and Zr while Cu concentration is significantly depleted from the surface and gradually increases with the sputtering in depth. The oxygen is reduced in content and decreases below 3 at% at around 200 s, indicating that the layer formed by pseudo-dealloying is about 20 nm thick. Fig. 3 (d) shows quantified AES analysis of the ribbon sample surfaces. The ratio of Cu/Ti on untreated ribbon was 0.3 while for both treated samples was 0.1 indicating evident removal of copper from the sample surface after

treatment. The FIB cut of etched 2 months ribbon sample showed dealloyed layer of thickness of about 20 nm (Fig. 4 SI) confirming the observations of AES study.

3.3. Contact angle measurement

The contact angle of untreated ribbon, etched 72 h, and etched 2 months ribbon was measured using 3 μL of deionized water. Table 1 shows that the wettability of the ribbons in deionized water increases from hydrophilic for untreated ribbon (contact angle of 75°) towards hydrophobic for etched 72 h ribbon (91°), and etched 2 months in between (Fig. 5 SI). All contact angle values are in the range between 75° and 91°, thus they follow Wenzel state of wetting which is the complete wetting of the rough surface with the liquid [61]. The surface free energy (SFE) can dictate the interaction of cells and bacteria with the surface of the material. It is discussed in the literature that high surface energy can promote cells and bacteria attachment while low surface energy can prevent bacteria adhesion [62,63]. Therefore, it is important to find a balance between maintaining SFE to promote cell attachment and prevent microbial growth [64]. The SFE was calculated starting from the measurement of contact angle of the sample surface with deionized water and di-iodomethane. Further, OWRK method was utilised for the SFE calculation, and the results are reported in Table 1. The etched 72 h and etched 2 months ribbon sample shows surface energy lower than untreated ribbon.

The average root mean square roughness (RMS) measured using AFM of untreated ribbon was 8.9 nm and etched 72 h was 1.8 nm (Fig. 6 SI), highlighting the change in the surface topography and wettability after the pseudo-dealloying treatment.

3.4. Hemolysis test

Hemocompatibility refers to the ability of an implant to interact with the blood cells without inducing an adverse reaction like hemolysis, which is the rupture of red blood cells [65,66]. The compatibility of the ribbons with blood is studied by evaluating the percentage of hemolysis using defibrinated sheep whole blood. Positive reference materials, i.e., quartz particles [67] and Mg alloy (WE43B) [68,69], and a negative reference material, i.e., cp-Ti [70] were included for comparison. ASTM F0756-17 (2017) considers material with percentage hemolysis less than 2% as hemocompatible [71].

Untreated and etched 72 h ribbons showed a very low hemolytic activity, not significantly different from the negative control (i.e., only PBS) (Fig. 4 (a)). Whereas Mg alloy showed 8% and quartz particle 24% of hemolysis indicating their significantly higher hemolytic activity. The ribbon samples before and after pseudo-dealloying showed percentage of hemolysis similar/lower than cp-Ti (i.e., 0.5% of hemolysis), indicating a safe range of hemolysis for these materials. The ribbons did not show evident Hb adsorption (Fig. 4 (b)), as the Hb absorbance of all the ribbons was comparable to the negative control, i.e., PBS. The results point towards the ability of ribbons to exhibit hemocompatibility after the pseudo-dealloying treatment and no significant interference due to adsorption of the Hb by the ribbons untreated and etched 72 h. This result is in line with previous findings on Ti/Zr-based amorphous alloys compositions such as $Zr_{56}Al_{16}Co_{28}$, $Zr_{53}Cu_{33}Al_9Ta_5$, and $Ti_{60}Nb_{15}Zr_{10}Si_{15}$ (at%), which reported no evidence of hemolysis and high hemocompatibility [56,72,73]. Several properties of the alloy may affect hemocompatibility, including surface chemical composition, roughness, hydrophilicity/hydrophobicity [55,74]. In this specific case, the hemocompatibility of the etched 72 h was not affected by the variation of the ribbon surface after the treatment.

Table 1
Wettability study on untreated and etched ribbons measured using deionized water (polar) and di-iodomethane (non-polar) solvent and calculated surface free energy (n = 9).

Samples	Contact angle Deionized Water (°)	Contact angle Diiodomethane (°)	SFE (mN/m)
Untreated Ribbon	76 ± 7	42 ± 6	43.7
Etched 72 h	92 ± 4	51 ± 3	35.2
Etched 2 months	85 ± 6	47 ± 4	38.5

3.5. Hydroxyl radical generation

The production of •OH radicals from the surface of the implanted material can be of great importance because material-induced •OH radical can boost intracellular oxidative stress with intense membrane lipid peroxidation that may lead to cell death [75]. However, a limited production of •OH radicals by the material can damage bacteria membranes, thus reducing biofilm formation and increasing the biocompatibility of the alloy [76,77]. Therefore, the production of •OH radicals was studied in a cell free media by mimicking cellular environment [78]. Untreated and etched 72 h ribbons were incubated for 10 min in PBS containing hydrogen peroxide to probe the release of •OH radicals when the ribbon samples were contacted in this oxidizing environment, which mimics what can be found in inflamed tissue. To unveil the mechanism of radical release, both the supernatant and the ribbon samples were assessed for •OH radical generation by using the DMPO spin trap molecule. DMPO is used to trap the released •OH radical to form DMPO-OH adduct, which is measured using EPR spectroscopy. The kinetic of DMPO-OH adduct formation was studied over a time of 0, 10, 30, and 60 min after adding DMPO. The test groups for instance in case of untreated sample were named as “Untreated: ribbon” and “Untreated: supernatant” and a similar terminology was used for etched 72 h sample. The results are shown in Fig. 5.

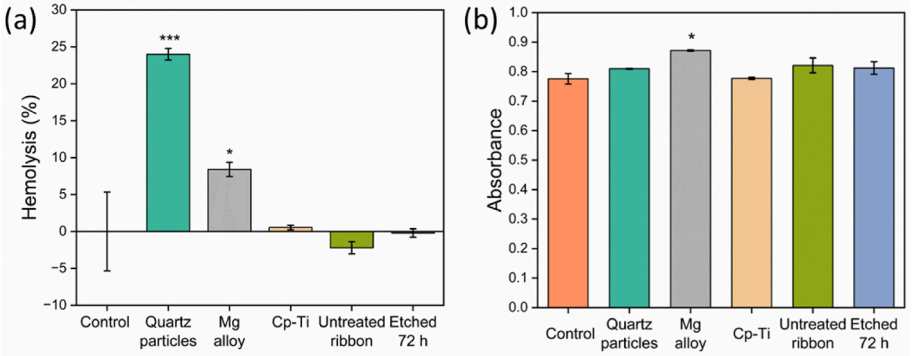

Fig. 4. (a) Percentage of hemolysis of untreated and etched 72 h ribbon incubated with defibrinated sheep blood, and (b) hemoglobin adsorption on the ribbons. Quartz particles and Mg alloy are used as positive reference materials, while Cp-Ti is used as negative reference material. Data are presented with mean ± SEM of three independent experiments and were analyzed with one-way ANOVA, followed by Dunnett's post-hoc test, sample vs control. *P < 0.05, ***P < 0.001.

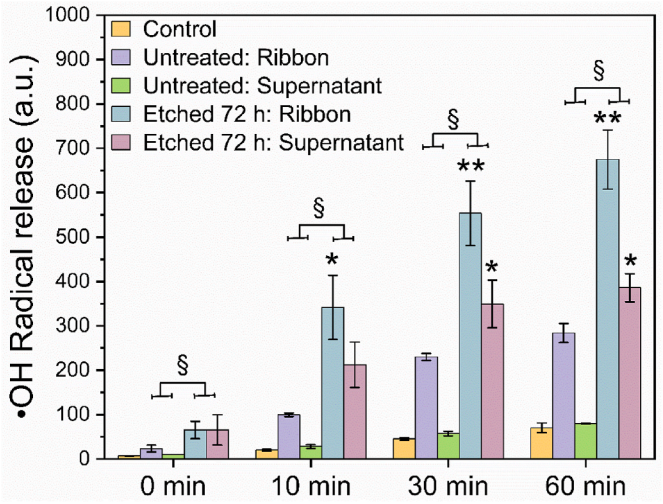

Fig. 5. •OH radical release after 10 min incubation of untreated and etched 72 h samples. The kinetic of DMPO-OH adduct formation was monitored over a time of 0, 10, 30, 60 min after adding DMPO. Radical release is calculated by double integration of the EPR spectra. Data are presented with mean ± SEM of two independent experiments and were analyzed with one-way ANOVA followed by Dunnett's post-hoc test, sample vs control, *P < 0.05, **P < 0.01. Two-way ANOVA was applied to compare (i) untreated vs etched 72 h ribbons, (ii) ribbon vs supernatant. P value of untreated vs etched 72 h samples: §P = 0.04; ribbon vs supernatant: no significant difference.

The results indicate that the production of •OH radical is significantly higher for the etched 72 h than the untreated sample, both for the ribbon and the supernatant. Moreover, for both untreated and etched 72 h, the production of •OH radicals were higher for the ribbon samples than only the supernatant. For the ribbon samples, the kinetic of DMPO-OH formation increased linearly with the incubation time. These results indicate that both the material surface and the transition metal ions leached from etched 72 h ribbon during 10 min incubation contribute to the production of •OH radical.

It is worth considering that the generation of •OH radicals may be attributed to two possible mechanisms.

(i). The presence of copper (Cu) atoms which could be trapped at the surface due to passivation of Ti/Zr rich sample surface during dealloying process. A similar observation was reported for $Au_{40}Cu_{28}Ag_7Pd_5Si_{20}$ amorphous alloy, wherein elements such as Cu, Ag and Pd were trapped in the ligaments [33,79]. This hypothesis gains support from the observed release of Cu ions from the etched 72 h sample discussed below in section 3.6. Furthermore, it is important to recognize that, although the reactivity of ions is greatly influenced by the nature of the matrix in which they are found [80] and by the environmental pH, isolated transition metal ions are often more chemically reactive than cluster ions. This has been observed for Fe [81] and Cu ions [80,82,83]. In this context, the accessible Cu ions present on the sample surface etched for 72 h could potentially be responsible for the observed increase in •OH radical.

(ii). The presence of a surface layer which is rich in titanium oxide. The reactivity of TiO_2 in releasing •OH radicals under irradiation has been extensively studied and it is well known. In recent years, research on the reactivity of TiO_2 in "dark" conditions has also grown steadily but, to date, only a few studies highlighted the release of •OH radicals in the dark by Ti-based materials [84]. Recently, Liu and colleagues reported that a TiO_2 nanostructured surface similar to an urchin can in situ reduce Ti^{4+} to Ti^{3+} in the presence of H_2O_2 to generate •OH radicals in the dark [85]. Similarly, Sanchez and colleagues detected •OH radicals and hydroperoxides in a TiO_2/H_2O_2 suspension not exposed to light [86]. Besides the presence of Ti(III) ions that can undergo the Fenton reaction [48,49], the •OH release in absence of light, may be ascribed to complexation of H_2O_2 on surface Ti(IV) leading generation of hydroperoxyl radicals (>Ti III–•OOH), through an inner-sphere electron transfer. The surface generated hydroperoxyl radical can further decompose to produce •OH radicals (eq (6)) [87–90].

$$Ti^{4+}–OOH \leftrightarrow Ti^{3+}–{}^{\bullet}OOH \quad (6)$$

As iron and other redox-active elements were not detected on the alloy surface (Fig. 3), their role in alloy reactivity was ruled out with respect to Cu and Ti.

3.6. Release of metal ions

Non biocompatible specimens that shows copper released from the surface of an implanted material in a limited concentration can contribute to the antibacterial activity of the surface while in high concentration, Cu ions can cause toxicity [91,92]. Examples reported in literature show that 46 mg/L Cu ions release resulted in LD50 value (lethal dose which kills 50% of the test population) for L929 fibroblasts, with nearly complete cell mortality observed at 100 mg/L [93] and a LD50 value of 18.4 mg/L Cu ions was observed for peripheral blood mononuclear cells (PBMCs) [94]. Therefore, it is of interest to investigate the ion release of the modified alloy in a cell culture media that mimic the environment of an implanted prosthesis allowing to detect the release of ions and to connect their concentration to the biocompatibility of the alloy.

Release of Ti and Cu from the untreated and etched 72 h ribbon after 3 days of incubation in the cell culture media was measured using ICP-MS. The release of titanium resulted to be below the detection limit of the technique for all samples. The copper ion released from untreated ribbons was 0.15 ± 0.09 mg/L, while 72 h ribbon was 0.06 ± 0.01 mg/L. It can be observed that untreated ribbon showed relatively high release of copper ions. It is important to note that the data of copper release from the surface of the untreated ribbons show high discrepancy among samples indicating the irregularities on the surface contributing to different amount of copper ion release, while the etched 72 h ribbon show higher consistency in the copper ion release from the surface. If compared to the literature data, it is possible to note that the amount of Cu ions released from the surface is far below the concentration reported to be lethal for cells. Therefore, it can be inferred that the limited Cu released can be helpful in the antibacterial activity while not detrimental for the cell adhesion to the surface.

3.7. Cytocompatibility of amorphous ribbons

Cytocompatibility investigation was performed on untreated and etched 72 h samples using Saos-2 and HOb cell lines. During cell culture, cells adhere and spread to the sample surface by forming focal contacts. As a general mechanism, in the initial stage they form a passive contact with the substrate or extracellular matrix (ECM) which later changes to complete spreading due to actin polymerization and distribution.

In the first step of cytocompatibility analysis, the ribbons (untreated and etched 72 h) cultured with Saos-2 cells were stained using calcein (green) for live cells and ethidium bromide (red) for dead cells after 3 days of incubation (Fig. 6 (a)). The results showed that cell viability of all samples was above 98%. In addition, the number of adhered live cells was higher on untreated ribbon with 63,146 ± 6,479 cells/cm^2, followed by etched 72 h sample with 55,880 ± 3,433 cells/cm^2 and then on glass control with 46,466 ± 10,070 cells/cm^2. These cytotoxicity results indicated that, despite the 40 at% copper content in the nominal composition of the amorphous ribbon, no cytotoxic effect was observed for both untreated and etched samples. Copper is generally considered a

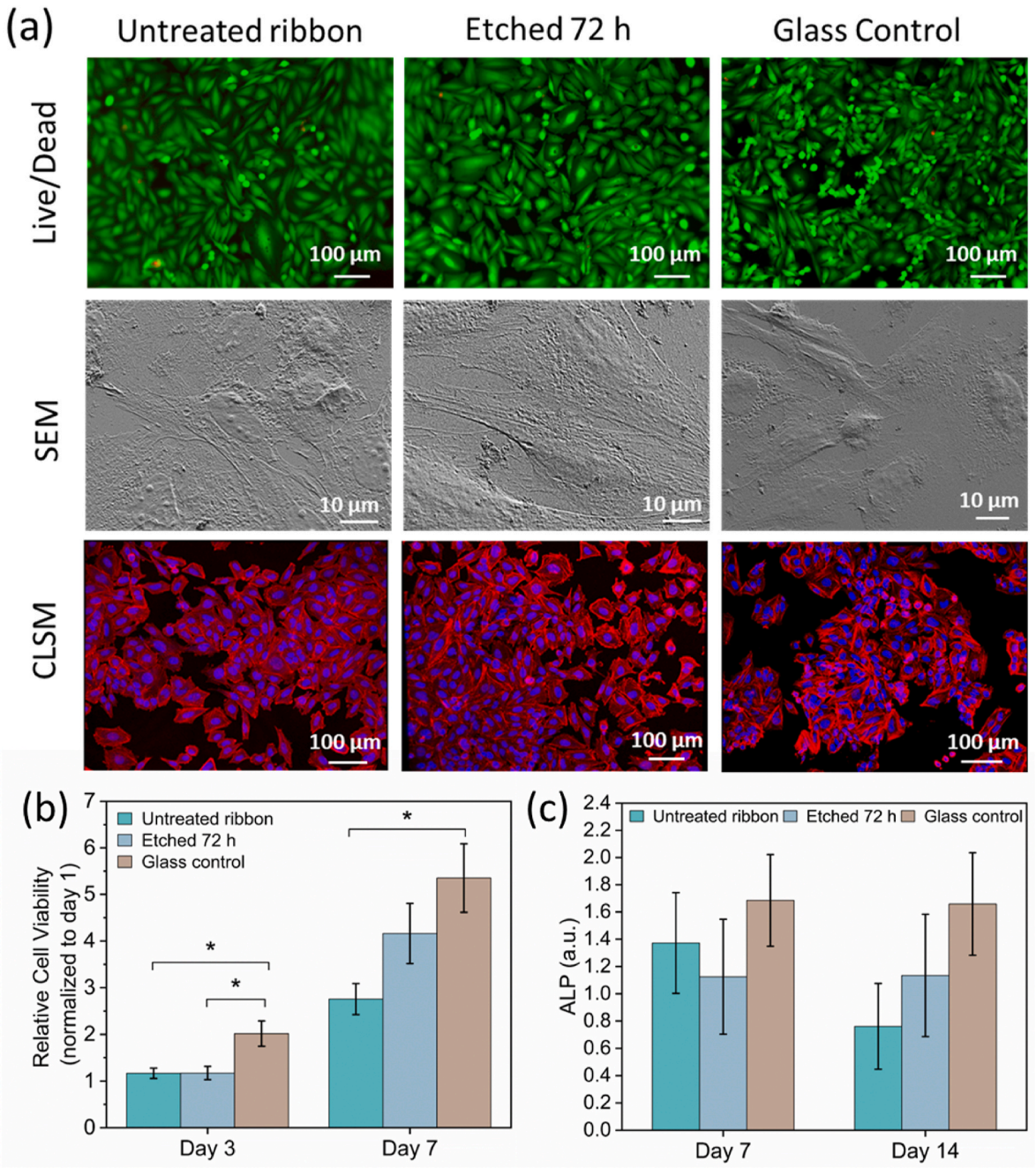

Fig. 6. (a) Representative images of Saos-2 cells grown on untreated ribbon, etched 72 h ribbon, and glass control stained using calcein (live/green) and ethidium dibromide (dead/red), SEM images of adhered cells showing the flat morphology, CLSM images of cells showing actin distribution (stress fibers/red) and nuclei (DNA/blue). (b) Cell proliferation measured using Alamar Blue after 1, 3, 7 days of culture. (c) ALP activity measured after 7, 14 days of culture. Data are represented with mean ± SEM of three independent experiments and were analyzed with one-way ANOVA, followed by Tukey's test for multiple comparison. *P < 0.05. (For interpretation of the references to colour in this figure legend, the reader is referred to the Web version of this article.)

toxic element and several authors have reported its deleterious effects on cell viability [95]. However, the potential cytotoxicity of copper is reduced when it is alloyed. Several studies have observed that osteoblasts can grow on alloys containing 38 at% of copper without showing any deleterious effect nor cytotoxicity [96]. Moreover, as described previously, the Cu released from the surface is limited and, therefore, it can be considered as not harmful for cells.

The morphology of the cells growing on samples showed cell material interaction and cell spreading. Cell morphology was studied using SEM after 3 days in culture. SEM images (Fig. 6 (a)) showed that osteoblasts were adhered to the analyzed surface exhibiting a flat appearance indicating good attachment. While in the untreated ribbon the presence of few rounded cells was detected, in the etched 72 h samples nearly all the cells were well spread on the surface with filopodia extensions in various directions, and several nucleoli in the nucleus of the cells were observed, indicating cell activity. The orientation and cytoskeleton distribution of the adhered cells were observed using CLSM (Fig. 6 (a)). Phalloidin was used to stain cytoskeletal actin fibers in red, and nuclei were counterstained in blue. For all the samples, well defined actin stress fibers, which were cross linked in the cytoskeleton of the cells, were observed, indicating good cell adhesion. The adhesion and morphology of cells growing on biomaterials is influenced by surface topography and wettability. Regarding etched 72 h sample, the topography showed hilly structures with a diameter of 18 ± 3 nm and distance

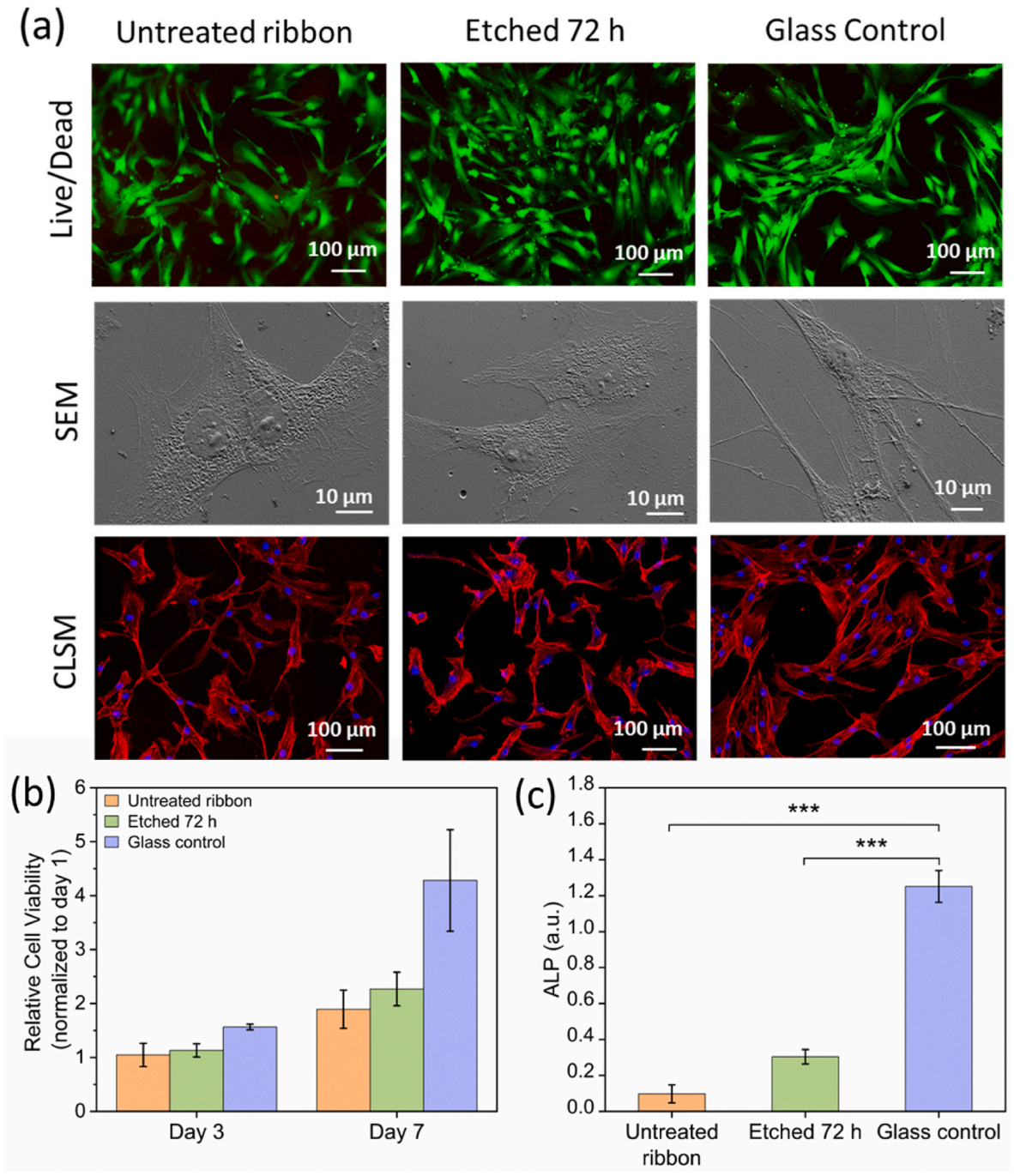

Fig. 7. (a) Representative images of HOb cells grown on untreated ribbon, etched 72 h ribbon, and glass control stained using calcein (live/green) and ethidium di bromide (dead/red), SEM images of adhered cells showing the flat appearance with long filipodia, CLSM images of cells showing the actin distribution (stress fibers, red) and nuclei (DNA, blue). (b) Cell proliferation measured using Alamar Blue after 1, 3, 7 days of culture. (c) ALP activity measured after 14 days of culture. Data are represented with mean ± SEM of three independent experiments and were analyzed with unpaired *t*-test or one-way ANOVA, followed by Tukey's test for multiple comparison. ***P < 0.001. (For interpretation of the references to colour in this figure legend, the reader is referred to the Web version of this article.)

between hills of 27 ± 7 nm. The nano roughness did not have any impact on cell adhesion and morphology. In addition, the contact angle of the treated ribbons was 91°. It is generally considered that the threshold for hydrophobicity is 90°. Thus, although the value is above the threshold to be considered hydrophilic, the results indicated that cells were able to spread on treated ribbons [97].

Fig. 6 (b) shows results of cell proliferation on the sample surface after 1, 3 and 7 days of incubation. No significant differences were observed between etched 72 h ribbons and untreated ribbons after 3 days of incubation. Additionally, no differences were found after 7 days in culture. After analyzing the proliferation of Saos-2 cells, the ability of cells to differentiate on samples was studied. To that end, ALP activity of osteoblast grown on ribbons was quantified after 7 and 14 days in culture (Fig. 6 (c)). After 7 days, the ALP activity was high on all samples with no significant differences among the samples. However, similar values were observed after 14 days in culture, indicating that ALP activity reached its maximum at day 7. The quantitative results for proliferation and ALP activity indicated that Saos-2 cells were able to grow and differentiate on both untreated and etched 72 h samples.

The same experiments previously performed on Saos2 cells were

Table 2
Condensed overview derived from the comprehensive analysis presented in this work on untreated and etched 72 h ribbons.

Sample			ROS	Saos-2 Cell			HOb Cell		
	Cu (mg/L)	Hemo compatibility	•OH Radical	Viability	Proliferation	Differentiation	Viability	Proliferation	Differentiation
Untreated Ribbon	↑	+++	+	+++	++	++	+++	++	+
Etched 72 h	↓	+++	+++	+++	++	++	+++	++	+

↑ High ↓ Low (+) Adequate (++) Good (+++) Very good.

done on HOb cells. In this case, the cells were not derived from a tumor but isolated from healthy donors. The cytotoxicity, cell morphology, and cell adhesion of HOb cells after 3 days of incubation is shown in Fig. 7 (a). Live and dead cells were evaluated on the samples after 3 days of culture. The samples showed cell viability above 96%. The number of live cells were similar on etched 72 h sample with 15,950 ± 3,859 cells/cm^2, glass control with 13,194 ± 2,244 cells/cm^2 and untreated ribbon samples with 10,423 ± 217 cells/cm^2. SEM images show that cells were well adhered to the sample surface. The filopodia were distributed in all directions indicating good cell spreading on the sample surface. Few dividing cells were observed and cells with several nuclei in the nucleus were also detected. CLSM images show well stained actin stress fibers in multiple directions throughout the cells indicating good cell adhesion on the sample surface. The results for cytotoxicity, morphology and adhesion of HOb were in agreement with the previous results observed for Saos-2 cells. The ribbons allowed cell adhesion, spreading without any cytotoxic effect. Fig. 7 (b) shows the result of cell proliferation on the sample surface after 3 and 7 days of culture. Both samples showed similar cell proliferation and no significant differences were observed between them. Regarding ALP activity quantification, as a cell differentiation parameter, all samples showed ALP activity after 14 days in culture (Fig. 7 (c)). No significant differences were observed between untreated and etched 72 h samples, although the ALP values of etched 72 h samples were slightly higher than untreated ones. ALP activity was not quantified in HOb cells after 7 days due to the low values obtained. HOb cells are undifferentiated cells that in order to differentiate need to be cultured under confluent conditions or under differentiated medium.

Evaluation of cytocompatibility using two cell lines of Saos-2 and HOb helped in understanding the cellular response of ribbon samples before and after pseudo-dealloying treatment. Infinite cell lines like Saos-2 cells are widely used for in vitro studies of materials for evaluation of the cytocompatibility. Saos-2 cell is a well characterized cell line that resembles HOb cells in most of the parameters analyzed, including adhesion and differentiation [98]. However, this cell model does not entirely resemble the primary osteoblast cells (HOb cells). The physiological phenotype of HOb is closer to the in vivo osteoblasts than the Saos-2 cells. Thus, a complementary result obtained from both cell lines enhances the knowledge to better understand their interaction with the untreated and etched ribbon samples.

4. Summary and conclusion

A new Ti based amorphous alloy with composition $Ti_{40}Cu_{40}Zr_{11}Fe_3Sn_3Ag_3$ was proposed as advanced material for the use as biomaterial. In this respect, a pseudo-dealloying process using HNO_3 as electrolyte was studied and optimized in order to: (i) to maximize the hemocompatibility and biocompatibility of the alloy, (ii) to allow •OH radical production from the surface that can enable an antibacterial activity of the surface and (iii) tailor the surface composition to enable Cu release from the surface in a limited amount in order to contribute to the antibacterial activity of the surface without having a harmful effect towards cells.

The findings from aforementioned investigations on untreated and etched 72 h ribbons are summarized in Table 2. It is important to note that treating the material with pseudo-dealloying improved the properties of the amorphous ribbon for instance enhancing the •OH generation activity of the etched 72 h sample, for possible antimicrobial response as compared to untreated ribbon. The presence of Cu ions released can validate the production of •OH radical from Cu atoms entrapped on the surface after pseudo-dealloying treatment that eventually can be released during the incubation. The overall results on cell proliferation and cell differentiation response of the etched 72 h sample with Saos-2 and HOb cells show high cytocompatibility and cell adhesion, being similar to untreated sample. Moreover, the amount of Cu released from the surface of untreated and etched 72 h ribbons can be considered limited enough and not harmful for the body.

In detail, the pseudo-dealloying treatement shows dependence on parameters such as temperature and time, on evolution of different surface morphologies on $Ti_{40}Cu_{40}Zr_{11}Fe_3Sn_3Ag_3$ amorphous alloy. Elevated temperature results in faster dissolution and formation of globular structures while lower temperature and longer immersion time results in formation of nanoporous morphology with ligaments and pores interconnected. The etched 72 h ribbon sample showed hydrophobic wettability and ability to boost release of •OH radical in a cell free system after 10 min of incubation with H_2O_2. Despite the radical capacity, the rate of hemolysis of the ribbons was comparable to cp-Ti indicating good hemocompatibility. In addition, the results of in vitro studies using Saos-2 and HOb cells showed a good biocompatibility for the etched 72 h ribbon. The etched 72 h ribbon was non-cytotoxic for Saos-2 and HOb cells, and showed good cell proliferation after 7 days of incubation. Early stage of osteogenic activity was also observed by the etched 72 h ribbon. Thus, overall, the HNO_3 etched $Ti_{40}Cu_{40}Zr_{11}Fe_3Sn_3Ag_3$ at% amorphous alloy showed promising biocompatible properties. The capacity of this material to induce •OH radical in a short time could possibly contribute towards limiting bacteria adhesion and biofilm formation on the surface. This work was focused on biocompatibility evaluations, and antibacterial activity studies would be performed to study the main advantageous properties of this new type of implantable materials.

Funding information

This work has received funding from the European Union's Horizon 2020 research and innovation programme under the Marie Skłodowska-Curie grant agreements No. 861046 (Bioremia European Training Networks), grant PID2020 116844RB-C22 funded by MCIN and 2021-SGR-00122 funded by the Generalitat de Catalunya, Deutsche Forschungsgemeinschaft (DFG) under the grant agreement No. 458057521; GE 1106/15-1 postdoctoral fellowship within the Beatriu de Pinós programme funded by the Secretary of Universities and Research (Government of Catalonia) and Horizon 2020 programme of research and innovation of the European Union under Marie Sklodowska-Curie grant agreement No. 801370. Authors acknowledge support from Project CH4.0 under the MUR program "Dipartimenti di Eccellenza 2023–2027" (CUP: D13C22003520001).

Declaration of competing interest

The authors declare that they have no known competing financial interests or personal relationships that could have appeared to influence the work reported in this paper.

Acknowledgment

The authors would like to thank the staff from the Servei de Microscòpia of Universitat Autònoma de Barcelona.

Appendix A. Supplementary data

Supplementary data to this article can be found online at https://doi.org/10.1016/j.jmrt.2024.03.225.

References

[1] Egami T, Iwashita T, Dmowski W. Mechanical properties of metallic glasses. Metals 2013;3:77–113. https://doi.org/10.3390/MET3010077. 3 (2013) 77–113.
[2] Li HF, Zheng YF. Recent advances in bulk metallic glasses for biomedical applications. Acta Biomater 2016;36:1–20. https://doi.org/10.1016/J.ACTBIO.2016.03.047.
[3] Schroers J, Kumar G, Hodges TM, Chan S, Kyriakides TR. Bulk metallic glasses for biomedical applications. JOM 2009;61:21–9. https://doi.org/10.1007/S11837-009-0128-1/METRICS.
[4] Zhu SL, Wang XM, Qin FX, Inoue A. A new Ti-based bulk glassy alloy with potential for biomedical application. Mater Sci Eng 2007;459:233–7. https://doi.org/10.1016/J.MSEA.2007.01.044.
[5] Liu Y, Wang G, Li H, Pang S, Chen K, Zhang T. TiCuZrFeSnSiSc bulk metallic glasses with good mechanical properties for biomedical applications. J Alloys Compd 2016;679:341–9. https://doi.org/10.1016/J.JALLCOM.2016.03.224.
[6] Zhu S, Wang X, Qin F, Inoue A. Glass-forming ability and thermal stability of Ti–Zr–Cu–Pd–Si bulk glassy alloys for biomedical applications. Mater Trans 2007;48:163–6. https://doi.org/10.2320/MATERTRANS.48.163.
[7] Zhu SL, Wang XM, Inoue A. Glass-forming ability and mechanical properties of Ti-based bulk glassy alloys with large diameters of up to 1 cm. Intermetallics 2008;16:1031–5. https://doi.org/10.1016/J.INTERMET.2008.05.006.
[8] Gao K, Zhu XG, Chen L, Li WH, Xu X, Pan BT, Li WR, Zhou WH, Li L, Huang W, Li Y. Recent development in the application of bulk metallic glasses. J Mater Sci Technol 2022;131:115–21. https://doi.org/10.1016/J.JMST.2022.05.028.
[9] Wang YB, Li HF, Cheng Y, Zheng YF, Ruan LQ. In vitro and in vivo studies on Ti-based bulk metallic glass as potential dental implant material. Mater Sci Eng C 2013;33:3489–97. https://doi.org/10.1016/J.MSEC.2013.04.038.
[10] Liu Y, Pang S, Li H, Hu Q, Chen B, Zhang T. Formation and properties of Ti-based Ti-Zr-Cu-Fe-Sn-Si bulk metallic glasses with different (Ti + Zr)/Cu ratios for biomedical application. Intermetallics 2016;72:36–43. https://doi.org/10.1016/j.intermet.2016.01.007.
[11] Yang W, Liu Y, Hua N, Pang S, Li Y, Liaw PK, Zhang T. Formation and properties of biocompatible Ti-based bulk metallic glasses in the Ti – Cu – Zr – Fe – Sn – Si – Ag system. J Non-Cryst Solids 2021;571:121060. https://doi.org/10.1016/j.jnoncrysol.2021.121060.
[12] Kokubun R, Wang W, Zhu S, Xie G, Ichinose S, Itoh S, Takakuda K. In vivo evaluation of a Ti-based bulk metallic glass alloy bar. Bio Med Mater Eng 2015;26:9–17. https://doi.org/10.3233/BME-151546.
[13] Demetriou MD, Wiest A, Hofmann DC, Johnson WL, Han B, Wolfson N, Wang G, Liaw PK. Amorphous metals for hard-tissue prosthesis. JOM 2010;62:83–91. https://doi.org/10.1007/S11837-010-0038-2/METRICS.
[14] Xue T, Attarilar S, Liu S, Liu J, Song X, Li L, Zhao B, Tang Y. Surface modification techniques of titanium and its alloys to functionally optimize their biomedical properties: thematic review. Front Bioeng Biotechnol 2020;8:1261. https://doi.org/10.3389/FBIOE.2020.603072/BIBTEX.
[15] Manivasagam VK, Popat KC. Hydrothermally treated titanium surfaces for enhanced osteogenic differentiation of adipose derived stem cells. Mater Sci Eng C 2021;128:112315. https://doi.org/10.1016/J.MSEC.2021.112315.
[16] Vishnu J, K Manivasagam V, Gopal V, Bartomeu Garcia C, Hameed P, Manivasagam G, Webster TJ. Hydrothermal treatment of etched titanium: a potential surface nano-modification technique for enhanced biocompatibility. Nanomedicine 2019;20:102016. https://doi.org/10.1016/J.NANO.2019.102016.
[17] Manivasagam VK, Perumal G, Arora HS, Popat KC. Enhanced antibacterial properties on superhydrophobic micro-nano structured titanium surface. J Biomed Mater Res 2022;110:1314–28. https://doi.org/10.1002/JBM.A.37375.
[18] Kurup A, Dhatrak P, Khasnis N. Surface modification techniques of titanium and titanium alloys for biomedical dental applications: a review. Mater Today Proc 2021;39:84–90. https://doi.org/10.1016/J.MATPR.2020.06.163.
[19] Pesode P, Barve S. Surface modification of titanium and titanium alloy by plasma electrolytic oxidation process for biomedical applications: a review. Mater Today Proc 2021;46:594–602. https://doi.org/10.1016/J.MATPR.2020.11.294.
[20] McCue I, Benn E, Gaskey B, Erlebacher J. Dealloying and dealloyed materials. Annu Rev Mater Res 2016;46:263–86. https://doi.org/10.1146/annurev-matsci-070115-031739.
[21] Vassileva E, Mihaylov L, Lyubenova L, Spassov T, Scaglione F, Rizzi P. Porous metallic structures by dealloying amorphous alloys. J Alloys Compd 2023;969:172417. https://doi.org/10.1016/J.JALLCOM.2023.172417.
[22] Hadden M, Martinez-Martin D, Yong KT, Ramaswamy Y, Singh G. Recent advancements in the fabrication of functional nanoporous materials and their biomedical applications. Materials 2022;15. https://doi.org/10.3390/ma15062111.
[23] Li J, Yu N, Jiang H, Leng J, Geng H. Effects of annealing temperature on dealloying of Ti – Cu Alloy. Corros Sci 2015;91:95–100. https://doi.org/10.1016/j.corsci.2014.11.002.
[24] Zhao Z, Xu J, Liaw PK, Wu B, Wang Y. One-step formation and photocatalytic performance of spindle-like TiO2 nanorods synthesized by dealloying amorphous Cu50Ti50 alloy. Corros Sci 2014;84:66–73. https://doi.org/10.1016/j.corsci.2014.03.014.
[25] Wang N, Pan Y, Wu S, Zhang E, Dai W. Rapid synthesis of rutile TiO 2 nano-flowers by dealloying Cu 60 Ti 30 Y 10 metallic glasses. Appl Surf Sci 2018;428:328–37. https://doi.org/10.1016/j.apsusc.2017.09.041.
[26] Wang W, Qiao Z, Zhao Y, Xie G, Yan S, Pang Z, Chen Y, Yang H, Zhang M, Zhang Y, Li W, Jiang Y, Yu Z, Zhang Z. SO42−-ion induced synthesis of 3D porous hydrangea-shaped anatase TiO2 as high performance anode material for lithium/sodium-ion batteries. J Porous Mater 2023;1:1–9. https://doi.org/10.1007/S10934-022-01416-W/FIGURES/7.
[27] Wang P, Yi X, Lu Y, Yu H, Yu J. In-situ synthesis of amorphous H2TiO3-modified TiO2 and its improved photocatalytic H2-evolution performance. J Colloid Interface Sci 2018;532:272–9. https://doi.org/10.1016/j.jcis.2018.07.139.
[28] Wang N, Pan Y, Dai W, Wu S, an Zhu Y, Zhang E. Dealloying synthesis of SnO 2 –TiO 2 solid solution and composite nanoparticles with excellent photocatalytic activity. Appl Surf Sci 2018;457:200–7. https://doi.org/10.1016/j.apsusc.2018.06.225.
[29] Zhu SL, He JL, Yang XJ, Cui ZD, Pi LL. Ti oxide nano-porous surface structure prepared by dealloying of Ti-Cu amorphous alloy. Electrochem Commun 2011;13:250–3. https://doi.org/10.1016/j.elecom.2010.12.025.
[30] Zhu S, Xie G, Yang X, Cui Z. A thick hierarchical rutile TiO2 nanomaterial with multilayered structure. Mater Res Bull 2013;48:1961–6. https://doi.org/10.1016/j.materresbull.2013.01.049.
[31] Zhu SL, He JL, Yang XJ, Cui ZD, Pi LL. Ti oxide nano-porous surface structure prepared by dealloying of Ti-Cu amorphous alloy. Electrochem Commun 2011;13:250–3. https://doi.org/10.1016/j.elecom.2010.12.025.
[32] Erlebacher J. Dealloying of silver/gold/(platinum) alloys. ECS Meeting Abstracts MA2007-02 2007:852. https://doi.org/10.1149/ma2007-02/13/852. 852.
[33] Paschalidou EM, Scaglione F, Gebert A, Oswald S, Rizzi P, Battezzati L. Partially and fully de-alloyed glassy ribbons based on Au: application in methanol electro-oxidation studies. J Alloys Compd 2016;667:302–9. https://doi.org/10.1016/j.jallcom.2016.01.181.
[34] Fernández-Navas N., Querebillo C.J., Tiwari K., Hantusch M., Shtefan V., Pérez N., Rizzi P., Zimmermann M., Gebert A. Electrochemical Surface Nanostructuring of Ti47cu38fe2.5zr7.5sn2si1ag2 Metallic Glass for Improved Corrosion Resistance, advanced engineering materials. Adv Eng Mater. Submitted for publication.
[35] Wang T, Wu YD, Si JJ, Cai YH, Chen XH, Hui XD. Novel Ti-based bulk metallic glasses with superior plastic yielding strength and corrosion resistance. Mater Sci Eng 2015;642:297–303. https://doi.org/10.1016/J.MSEA.2015.05.060.
[36] Zhu ZW, Zhang HF, Sun WS, Hu ZQ. Effect of Zr addition on the glass-forming ability and mechanical properties of Ni–Nb alloy. J Mater Res 2007;22:453–9. https://doi.org/10.1557/JMR.2007.0055.
[37] Li DK, Zhang HF, Wang AM, Zhu ZW, Hu ZQ. Effect of Sn addition on the glass-forming ability and mechanical properties of Ni-Nb-Zr bulk metallic glasses. Chin Sci Bull 2011;56:3926–31. https://doi.org/10.1007/S11434-011-4763-X/METRICS.
[38] Bai L, Ding Z, Zhang H, Cui C. Glass-forming ability and corrosion behavior of Ti-based amorphous alloy Ti-Zr-Si-Fe. Materials 2022;15:7229. https://doi.org/10.3390/MA15207229. Page 7229 15 (2022).
[39] Zhang M, Song YQ, Lin HJ, Li Z, Li W. A brief introduction on the development of Ti-based metallic glasses. Front Mater 2022;8:814629. https://doi.org/10.3389/FMATS.2021.814629/BIBTEX.
[40] Pang S, Liu Y, Li H, Sun L, Li Y, Zhang T. New Ti-based Ti–Cu–Zr–Fe–Sn–Si–Ag bulk metallic glass for biomedical applications. J Alloys Compd 2015;625:323–7. https://doi.org/10.1016/J.JALLCOM.2014.07.021.
[41] Liu Y, Pang S, Yang W, Hua N, Liaw PK, Zhang T. Tribological behaviors of a Ni-free Ti-based bulk metallic glass in air and a simulated physiological environment. J Alloys Compd 2018;766:1030–6. https://doi.org/10.1016/j.jallcom.2018.07.023.
[42] Yang W, Liu Y, Hua N, Pang S, Li Y, Liaw PK, Zhang T. Formation and properties of biocompatible Ti-based bulk metallic glasses in the Ti–Cu–Zr–Fe–Sn–Si–Ag system. J Non-Cryst Solids 2021;571:121060. https://doi.org/10.1016/j.jnoncrysol.2021.121060.
[43] Gostin PF, Addison O, Morrell AP, Zhang Y, Cook AJMC, Liens A, Stoica M, Ignatyev K, Street SR, Wu J, Chiu YL, Davenport AJ. In situ synchrotron X-ray diffraction characterization of corrosion products of a Ti-based metallic glass for implant applications. Adv Healthc Mater 2018;7. https://doi.org/10.1002/ADHM.201800338.
[44] Gostin PF, Eigel D, Grell D, Eckert J, Kerscher E, Gebert A. Comparing the pitting corrosion behavior of prominent Zr-based bulk metallic glasses. J Mater Res 2015;30:233–41. https://doi.org/10.1557/JMR.2014.371.
[45] Fornell J, Pellicer E, Van Steenberge N, González S, Gebert A, Suriñach S, Baró MD, Sort J. Improved plasticity and corrosion behavior in Ti–Zr–Cu–Pd metallic glass with minor additions of Nb: an alloy composition intended for biomedical applications. Mater Sci Eng 2013;559:159–64. https://doi.org/10.1016/J.MSEA.2012.08.058.
[46] Qin FX, Xie GQ, Wang XM, Wada T, Song M, Furuya K, Yoshimura M, Tsukamoto M, Inoue A. Microstructure and electrochemical properties of PVD TiN, (Ti, Al) N-coated Ti-based bulk metallic glasses. Mater Trans 2009;50:1313–7. https://doi.org/10.2320/MATERTRANS.ME200820.

[47] Weidinger A, Kozlov AV. Biological activities of reactive oxygen and nitrogen species: oxidative stress versus signal transduction. Biomolecules 2015;5:472–84. https://doi.org/10.3390/BIOM5020472. 5 (2015) 472–484.
[48] Brooks E, Tobias M, Krautsak K, Ehrensberger M. The influence of cathodic polarization and simulated inflammation on titanium electrochemistry. J Biomed Mater Res B Appl Biomater 2014;102:1445–53. https://doi.org/10.1002/JBM.B.33123.
[49] Prestat M, Thierry D. Corrosion of titanium under simulated inflammation conditions: clinical context and in vitro investigations. Acta Biomater 2021;136:72–87. https://doi.org/10.1016/J.ACTBIO.2021.10.002.
[50] Xia T, Kovochich M, Liong M, Mädler L, Gilbert B, Shi H, Yeh JI, Zink JI, Nel AE. Comparison of the mechanism of toxicity of zinc oxide and cerium oxide nanoparticles based on dissolution and oxidative stress properties. ACS Nano 2008;2:2121–34. https://doi.org/10.1021/NN800511K/SUPPL_FILE/NN800511K_SI_001.PDF.
[51] Rajan ST, Arockiarajan A. Thin film metallic glasses for bioimplants and surgical tools: a review. J Alloys Compd 2021;876:159939. https://doi.org/10.1016/J.JALLCOM.2021.159939.
[52] Ye J, Li B, Li M, Zheng Y, Wu S, Han Y. ROS induced bactericidal activity of amorphous Zn-doped titanium oxide coatings and enhanced osseointegration in bacteria-infected rat tibias. Acta Biomater 2020;107:313–24. https://doi.org/10.1016/J.ACTBIO.2020.02.036.
[53] Wang YB, Li HF, Cheng Y, Zheng YF, Ruan LQ. In vitro and in vivo studies on Ti-based bulk metallic glass as potential dental implant material. Mater Sci Eng C 2013;33:3489–97. https://doi.org/10.1016/J.MSEC.2013.04.038.
[54] Cerqueni G, Scalzone A, Licini C, Gentile P, Mattioli-Belmonte M. Insights into oxidative stress in bone tissue and novel challenges for biomaterials. Mater Sci Eng C 2021;130:112433. https://doi.org/10.1016/J.MSEC.2021.112433.
[55] Catanio Bortolan C, Copes F, Shekargoftar M, de Oliveira Fidelis Sales V, Paternoster C, Contri Campanelli L, Giguère N, Mantovani D. Electrochemical and in vitro biological behaviors of a Ti-Mo-Fe alloy specifically designed for stent applications. Biomaterials and Biosystems 2023;10:100076. https://doi.org/10.1016/J.BBIOSY.2023.100076.
[56] Thanka Rajan S, Bendavid A, Subramanian B. Cytocompatibility assessment of Ti-Nb-Zr-Si thin film metallic glasses with enhanced osteoblast differentiation for biomedical applications. Colloids Surf B Biointerfaces 2019;173:109–20. https://doi.org/10.1016/J.COLSURFB.2018.09.041.
[57] Zhu S, Xie G, Yang X, Cui Z. A thick hierarchical rutile TiO2 nanomaterial with multilayered structure. Mater Res Bull 2013;48:1961–6. https://doi.org/10.1016/J.MATERRESBULL.2013.01.049.
[58] Scaglione F, Gebert A, Battezzati L. Dealloying of an Au-based amorphous alloy. Intermetallics 2010;18:2338–42. https://doi.org/10.1016/j.intermet.2010.08.005.
[59] Gao H, Li Z, Zhou S, Zhang G, Cui N. The improvement of surface quality and thickness stability of Fe78Si9B13 melt-spun ribbons by melt overheating. Prog Nat Sci: Mater Int 2019;29:556–60. https://doi.org/10.1016/J.PNSC.2019.08.012.
[60] Scaglione F, Rizzi P, Celegato F, Battezzati L. Synthesis of nanoporous gold by free corrosion of an amorphous precursor. J Alloys Compd 2014;615:S142–7. https://doi.org/10.1016/J.JALLCOM.2014.01.239.
[61] Fan H, Guo Z. Bioinspired surfaces with wettability: biomolecule adhesion behaviors. Biomater Sci 2020;8:1502–35. https://doi.org/10.1039/c9bm01729a.
[62] Zheng S, Bawazir M, Dhall A, Kim HE, He L, Heo J, Hwang G. Implication of surface properties, bacterial motility, and hydrodynamic conditions on bacterial surface sensing and their initial adhesion. Front Bioeng Biotechnol 2021;9:1–22. https://doi.org/10.3389/fbioe.2021.643722.
[63] Gittens RA, Scheideler L, Rupp F, Hyzy SL, Geis-Gerstorfer J, Schwartz Z, Boyan BD. A review on the wettability of dental implant surfaces II: biological and clinical aspects. Acta Biomater 2014;10:2907–18. https://doi.org/10.1016/j.actbio.2014.03.032.
[64] Gittens RA, Scheideler L, Rupp F, Hyzy SL, Geis-Gerstorfer J, Schwartz Z, Boyan BD. A review on the wettability of dental implant surfaces II: biological and clinical aspects. Acta Biomater 2014;10:2907–18. https://doi.org/10.1016/j.actbio.2014.03.032.
[65] Osorio M, Cañas A, Puerta J, Díaz L, Naranjo T, Ortiz I, Castro C. Ex vivo and in vivo biocompatibility assessment (blood and tissue) of three-dimensional bacterial nanocellulose biomaterials for soft tissue implants. Sci Rep 2019;9:1–9. https://doi.org/10.1038/s41598-019-46918-x (2019) 1–14.
[66] Manivasagam VK, Popat KC. Improved hemocompatibility on superhemophobic micro–nano-structured titanium surfaces. Bioengineering 2023;10:43. https://doi.org/10.3390/BIOENGINEERING10010043. Page 43 10 (2022).
[67] Pavan C, Sydor MJ, Bellomo C, Leinardi R, Cananà S, Kendall RL, Rebba E, Corno M, Ugliengo P, Mino L, Holian A, Turci F. Molecular recognition between membrane epitopes and nearly free surface silanols explains silica membranolytic activity. Colloids Surf B Biointerfaces 2022;217:112625. https://doi.org/10.1016/J.COLSURFB.2022.112625.
[68] Fu J, Su Y, Qin Y, Zheng Y, Wang Y, Zhu D. Biomaterials Evolution of metallic cardiovascular stent materials : a comparative study among stainless steel , magnesium and zinc. Biomaterials 2020;230:119641. https://doi.org/10.1016/j.biomaterials.2019.119641.
[69] Manivasagam VK, Sankar M, Caterina, Garcia B, Vishnu J, Chatterjee Kaushik, Suwas Satyam, Manivasagam G, Thomas, Webster J, Garcia CB, Chatterjee K, Suwas S, Webster TJ. Surface-modified WE43 magnesium alloys for reduced degradation and superior biocompatibility. Models 2022;1(3 1):273–88. https://doi.org/10.1007/S44164-022-00016-X. 2022.
[70] Manivasagam VK, Popat KC. In vitro investigation of hemocompatibility of hydrothermally treated titanium and titanium alloy surfaces. ACS Omega 2020;5:8108–20. https://doi.org/10.1021/acsomega.0c00281.
[71] F756 Standard Practice for Assessment of Hemolytic Properties of Materials, (n.d.). https://www.astm.org/f0756-17.html (accessed November 28, 2023).
[72] Bai MY, Chang YC, Chu JP. Preclinical studies of non-stick thin film metallic glass-coated syringe needles. Sci Rep 2020;10:1–11. https://doi.org/10.1038/s41598-020-77008-y.
[73] Wang R, Wang Y, Yang J, Sun J, Xiong L. Influence of heat treatment on the mechanical properties, corrosion behavior, and biocompatibility of Zr56Al16Co28 bulk metallic glass. J Non-Cryst Solids 2015;411:45–52. https://doi.org/10.1016/J.JNONCRYSOL.2014.12.018.
[74] Manivasagam VK, Sabino RM, Kantam P, Popat KC. Surface modification strategies to improve titanium hemocompatibility: a comprehensive review. Mater Adv 2021;2:5824–42. https://doi.org/10.1039/d1ma00367d.
[75] Zhou D, Shao L, Spitz DR. Reactive oxygen species in normal and tumor stem cells. Adv Cancer Res 2014;122:1–67. https://doi.org/10.1016/B978-0-12-420117-0.00001-3.
[76] Yang HL, Zou L, Juaim AN, Ma CX, Zhu MZ, Xu F, Chen XN, Wang YZ, Zhou XW. Copper release and ROS in antibacterial activity of Ti-Cu alloys against implant-associated infection. Rare Met 2023;42:2007–19. https://doi.org/10.1007/s12598-022-02242-4.
[77] Mouthuy PA, Snelling SJB, Dakin SG, Milković L, Gašparović AČ, Carr AJ, Žarković N. Biocompatibility of implantable materials: an oxidative stress viewpoint. Biomaterials 2016;109:55–68. https://doi.org/10.1016/j.biomaterials.2016.09.010.
[78] Scarcello E, Herpain A, Tomatis M, Turci F, Jacques PJ, Lison D. Hydroxyl radicals and oxidative stress: the dark side of Fe corrosion. Colloids Surf B Biointerfaces 2020;185:110542. https://doi.org/10.1016/j.colsurfb.2019.110542.
[79] Scaglione F, Celegato F, Rizzi P, Battezzati L. A comparison of de-alloying crystalline and amorphous multicomponent Au alloys. Intermetallics 2015;66:82–7. https://doi.org/10.1016/J.INTERMET.2015.06.022.
[80] Li J, Pham AN, Dai R, Wang Z, Waite TD. Recent advances in Cu-Fenton systems for the treatment of industrial wastewaters: role of Cu complexes and Cu composites. J Hazard Mater 2020;392. https://doi.org/10.1016/J.JHAZMAT.2020.122261.
[81] Turci F, Tomatis M, Lesci IG, Roveri N, Fubini B. The iron-related molecular toxicity mechanism of synthetic asbestos nanofibres: a model study for high-aspect-ratio nanoparticles. Chemistry 2011;17:350–8. https://doi.org/10.1002/CHEM.201001893.
[82] Pachamuthu MP, Karthikeyan S, Maheswari R, Lee AF, Ramanathan A. Fenton-like degradation of Bisphenol A catalyzed by mesoporous Cu/TUD-1. Appl Surf Sci 2017;393:67–73. https://doi.org/10.1016/J.APSUSC.2016.09.162.
[83] Yashnik SA, Taran OP, Surovtsova TA, Ayusheev AB, Parmon VN. Cu- and Fe-substituted ZSM-5 zeolite as an effective catalyst for wet peroxide oxidation of Rhodamine 6 G dye. J Environ Chem Eng 2022;10:107950. https://doi.org/10.1016/J.JECE.2022.107950.
[84] Applications B, Zhou W, Gulino A, Querebillo CJ. A review on nano Ti-based oxides for dark and photocatalysis: from photoinduced processes to bioimplant applications. Nanomaterials 2023;13:982. https://doi.org/10.3390/NANO13060982. Page 982 13 (2023).
[85] Liu Z, Wang T, Yu X, Geng Z, Sang Y, Liu H. In situ alternative switching between Ti4+ and Ti3+ driven by H2O2 in TiO2 nanostructures: mechanism of pseudo-Fenton reaction. Mater Chem Front 2017;1:1989–94. https://doi.org/10.1039/C7QM00163K.
[86] Sánchez LD, Taxt-Lamolle SFM, Hole EO, Krivokapić A, Sagstuen E, Haugen HJ. TiO2 suspension exposed to H2O2 in ambient light or darkness: degradation of methylene blue and EPR evidence for radical oxygen species. Appl Catal, B 2013;142–143:662–7. https://doi.org/10.1016/J.APCATB.2013.05.017.
[87] Shetti VN, Manikandan P, Srinivas D, Ratnasamy P. Reactive oxygen species in epoxidation reactions over titanosilicate molecular sieves. J Catal 2003;216:461–7. https://doi.org/10.1016/S0021-9517(02)00119-7.
[88] Tengvall P, Lundström I, Sjöqvist L, Elwing H, Bjursten LM. Titanium-hydrogen peroxide interaction: model studies of the influence of the inflammatory response on titanium implants. Biomaterials 1989;10:166–75. https://doi.org/10.1016/0142-9612(89)90019-7.
[89] Kim DH, Bokare AD, Koo MS, Choi W. Heterogeneous catalytic oxidation of As(III) on nonferrous metal oxides in the presence of H2O2. Environ Sci Technol 2015;49:3506–13. https://doi.org/10.1021/ES5056897.
[90] Kim HH, Lee H, Lee D, Ko YJ, Woo H, Lee J, Lee C, Pham ALT. Activation of hydrogen peroxide by a titanium oxide-supported iron catalyst: evidence for surface Fe(IV) and its selectivity. Environ Sci Technol 2020;54:15424–32. https://doi.org/10.1021/ACS.EST.0C04262.
[91] Mahmoudi P, Akbarpour MR, Lakeh HB, Jing F, Hadidi MR, Akhavan B. Antibacterial Ti–Cu implants: a critical review on mechanisms of action. Mater Today Bio 2022;17:100447. https://doi.org/10.1016/j.mtbio.2022.100447.
[92] Chang SH, Chen BY, Lin JX. Toxicity assessment and selective leaching characteristics of Cu-Al-Ni shape memory alloys in biomaterials applications. J Appl Biomater Funct Mater 2016;14:e59–64. https://doi.org/10.5301/jabfm.5000245.
[93] Cao B, Zheng Y, Xi T, Zhang C, Song W, Burugapalli K, Yang H, Ma Y. Concentration-dependent cytotoxicity of copper ions on mouse fibroblasts in vitro: effects of copper ion release from TCu380A vs TCu220C intra-uterine devices. Biomed Microdevices 2012;14:709–20. https://doi.org/10.1007/S10544-012-9651-X.
[94] Singh RP, Kumar S, Nada R, Prasad R. Evaluation of copper toxicity in isolated human peripheral blood mononuclear cells and it's attenuation by zinc: ex vivo. Mol Cell Biochem 2006;282:13–21. https://doi.org/10.1007/S11010-006-1168-2.

[95] Yamamoto A, Honma R, Sumita M. Cytotoxicity evaluation of 43 metal salts using murine fibroblasts and osteoblastic cells. J Biomed Mater Res 1998;39:331–40. https://doi.org/10.1002/(SICI)1097-4636(199802)39:2.

[96] Blanquer A, Pellicer E, Hynowska A, Barrios L, Ibáñez E, Baró MD, Sort J, Nogués C. In vitro biocompatibility assessment of Ti40Cu38Zr10Pd12 bulk metallic glass. J Mater Sci Mater Med 2014;25:163–72. https://doi.org/10.1007/S10856-013-5041-Z.

[97] Wei J, Igarashi T, Okumori N, Igarashi T, Maetani T, Liu B, Yoshinari M. Influence of surface wettability on competitive protein adsorption and initial attachment of osteoblasts. Biomedical Materials 2009;4:045002. https://doi.org/10.1088/1748-6041/4/4/045002.

[98] Czekanska EM, Stoddart MJ, Ralphs JR, Richards RG, Hayes JS. A phenotypic comparison of osteoblast cell lines versus human primary osteoblasts for biomaterials testing. J Biomed Mater Res 2014;102:2636–43. https://doi.org/10.1002/JBM.A.34937.